Dynamics of solidification microstructure formation in DECLIC-DSI onboard ISS: dendritic patterns data treatment

Fatima L Mota, Mehdi Medjkoune, Kaihua Ji, Louise Strutzenberg Littles, Rohit Trivedi, Alain Karma, Nathalie Bergeon

Fatima L Mota, Mehdi Medjkoune, Kaihua Ji, Louise Strutzenberg Littles, Rohit Trivedi, et al.. Dynamics of solidification microstructure formation in DECLIC-DSI onboard ISS: dendritic patterns data treatment. International Astronautical Congress, Sep 2022, paris, France. hal-03824145

HAL Id: hal-03824145
https://hal.science/hal-03824145v1

IAC-22,A2,6,x67562

Dynamics of solidification microstructure formation in DECLIC-DSI onboard ISS: dendritic patterns data treatment

F.L. Mota[1*], M. Medjkoune[1], K. Ji[2], L. Strutzenberg Littles[3], R. Trivedi[4], A. Karma[2], N. Bergeon[1]

[1]*IM2NP, Aix-Marseille Université and CNRS, Marseille, France*
[2]*Physics Department, Northeastern University, Boston, USA*
[3]*Marshall Space Flight Center, Huntsville, USA*
[4]*Department of Materials Science & Engineering, Iowa State University, USA*
* Corresponding Author

Abstract

The study of solidification microstructure formation is of utmost importance for the design and processing of materials, as solid-liquid interface patterns largely govern the mechanical and physical properties of the resulting solid. Microstructure pattern selection occurs under dynamic conditions of growth in which the initial morphological instability evolves nonlinearly and undergoes a reorganization process. This dynamic and nonlinear nature renders in situ observation of the solid-liquid interface an invaluable tool for gaining knowledge on the time-evolution of the interface pattern in order to establish benchmark comparisons with the predictions of computational models. Transparent organic analogs, which solidify like metallic alloys, lend themselves to this type of observation, and have become the materials of choice for the direct study of interface dynamics. Extensive ground-based studies of both metallic and organic bulk samples have established that gravity causes significant and disruptive convection during solidification, which alters the microstructure formation. A reduced-gravity environment is therefore mandatory to render the convective flow effects negligible in bulk samples. Experiments were carried out in the Direct Solidification Insert (DSI) of the Device for the study of Critical Liquids and Crystallization (DECLIC) installed onboard the ISS. The DSI offered the unique opportunity to observe in situ and characterize the entire development of the microstructure in extended 3D patterns under diffusive growth conditions, using bulk samples of transparent organic alloys. Between 2010 and 2011, the first space campaign explored the entire range of microstructures resulting in unprecedented observations related to cellular patterns. A second campaign (DSI-R), performed between 2017 and 2018, expanded the benchmark database, particularly in the dendritic regime. In DSI-R, the alloy solute concentration was increased, leading to the formation of well-developed dendritic patterns. Interpretation of the images produced by these experiments necessitates a robust identification of each dendrite position and size during the whole solidification. We have developed several image analysis methods to achieve this goal reliably despite varying contrast and noise levels. Here, we present a typical solidification experiment and analyze the dynamics of the dendritic pattern formation to illustrate the application of the image analysis methods.

Keywords: DECLIC, Solidification, microgravity, image treatment.

Nomenclature

G: thermal gradient
L: solidified length
V: pulling velocity
V_d: drift velocity
λ: primary spacing
θ_g: angle between growth velocity and interface velocity

Acronyms/Abbreviations

CADMOS: Centre d'Aide au Développement des activités en Micro-pesanteur et des Opérations Spatiales
CNES: Centre National d'Études Spatiales
DBSCAN: Density-Based Spatial Clustering of Applications with Noise
DECLIC: Device for the study of Critical LIquids and Crystallization
DSI: Directional Solidification Insert
DSI-R: Directional Solidification Insert - Reflight
FFT: Fast Fourier Transform
ISS: International Space Station
NASA: National Aeronautics and Space Administration
SCN: Succinonitrile
3D: three-dimensional

1. Introduction

The study of solidification microstructure formation and selection is crucial for the engineering and processing of advanced new materials. The most typical microstructures are cells and dendrites, which form the interface solidification patterns that largely govern the mechanical and physical properties of materials. The evolution of these microstructures occurs under dynamic conditions, in which the pattern self-organizes into a rather periodic array. Therefore, in situ and real-time observation of the solid-liquid interface is an important tool for studying the time evolution of the interface. In light of this, transparent organic analogs that behave like metallic alloys are extensively used.

Unfortunately, the strong influence of convection on the solidification interface is a critical impediment in the study of three-dimensional (3D) pattern evolution in ground-based experiments. Extensive ground-based studies carried out in metallic and organic bulk samples have clearly established that fluid flow modifies the solute boundary layer, influencing the pattern development [1-3].

Directional solidification experiments under low gravity conditions provide a unique framework to investigate microstructure development in spatially extended sample geometries, with negligible convection effects and under well-controlled conditions of growth rate, temperature gradient, and alloy composition. The study presented here was conducted using the DSI dedicated to *in situ* and real-time characterization of the dynamical selection of the solid-liquid interface morphology in *bulk* samples of transparent materials, which was developed by the French Space Agency (CNES) in the frame of the DECLIC project. The DECLIC facility of CNES was launched for the first time with 17-A shuttle flight (August 2009) as part of a joint NASA/CNES research program and is installed on the International Space Station (ISS) in a microgravity environment. The main instrument monitoring is performed from the CADMOS in Toulouse. Taking advantage of provided tele-science capabilities, scientists have the ability to follow and remotely control experiments. The DSI was commissioned in December 2009, and 51 experiments during six runs of two to three weeks each were performed from April 2010 to April 2011. The DSI was then brought back on ground, and two runs of two weeks each were performed: the control parameters were similar to those used in microgravity so that convection influence could be addressed [3, 4]. After a sample change, a second flight campaign (DSI-R) was performed from October 2017 to November 2018: 50 experiments during six runs of three weeks each. Three additional runs of three weeks will be performed current 2022. This paper will be focused on results obtained during DSI-R, mostly dedicated to dendritic patterns.

The result of each experiment is a huge number of images that have to be analyzed to quantitatively characterize the dendritic pattern and its time evolution. In this article, we will focus on the method of data treatments that had to be developed to tackle these image sequences. In section 2, we will briefly introduce the experimental framework. In section 3, we will present specific image procedures and algorithms that we have developed to systematically analyze the experimental data in spite of their variability. In section 4, an example of analysis will be conducted on a typical experiment.

2. Experimental Framework

Essentially, the DECLIC-DSI insert consists of two elements: the Bridgman furnace and the experimental cartridge. More thorough descriptions of DECLIC and its inserts can be found in [5, 6].

The experimental cartridge includes a quartz crucible and a system of volume compensation made of stainless steel that is useful to accommodate the sample volume variations associated with phase changes. The cylindrical crucible has an inner diameter of 10 mm and a length that enables about 10 cm of solidification, allowing the study of the entire development of extended 3D patterns, from the initial stage to the steady-state. The crucible is equipped with a flat glass window at the bottom and a lens immersed in the melt at the top.

The cartridge was filled under vacuum with a succinonitrile (SCN) – 0.46 wt% camphor alloy, using SCN purified by NASA through distillation and zone melting. Once sealed, the cartridge was inserted into the Bridgman furnace. A monocrystalline seed with a direction <100> parallel to the pulling axis was prepared on the ground and kept unmelted during all the experimental campaigns.

The hot and cold zones of the Bridgman furnace were set up in a way to impose a thermal gradient ranging from 10 to 30 $K\cdot cm^{-1}$ and to maintain the solid-liquid interface in the adiabatic area located between the cold and hot zones. During the experiment, the crucible is pulled down from the hot zone into the cold zone at a rate ranging from 0.1 to 30 µm/s. For a given alloy concentration, we can set either the thermal gradient or, more conveniently, the pulling rate to create various interface morphologies, ranging from planar front to cellular and finally dendritic pattern.

A schematic of the apparatus is given in Fig. 1. The experimental cartridge is reduced to a cylinder with liquid on top and solid at the bottom. The main observation mode (axial observation) takes advantage of the complete axial transparency of the cartridge: the light coming from LEDs (noted LED A) passes through the cartridge from the bottom to the top, therefore crossing the interface. The optical imaging system formed by the immersed lens and the following relay lens forms the image of the interface on a CCD camera (noted CCD A). On the same cartridge axis, a He-Ne Mach-Zehnder interferometer is also present [7, 8]. The interface can also be observed from the side (transverse observation) using the LEDs and CCD camera both noted “T”.

During solidification, as the dendrite tips advance, they leave long irregular columns behind. These columns can be thought of as light waveguides, and parts of the tip surface that are more normal to the optical axis generally appear lighter, while the valleys between dendrites, which are farther from the normal, appear darker. However, the complex optical system that emerges during solidification introduces unpredictable brightness variations, such as bright spots between dendrites, and areas of low contrast (see, for example, Fig. 3a).

The resulting raw data are a sequence of images of the interface during solidification, including the onset and stabilization of the solidification front. To study the microstructural evolution of the solidification interface, we characterize each dendrite in terms of its position on the interface and its size. The analysis of axial images therefore requires several steps. Starting from axial images, a binary mask is created to label each dendrite separately, and to calculate its center position. The corresponding procedures will be explained in sections 3.1 and 3.2. A Voronoi tessellation of these points is then used to identify the first neighbors of each dendrite at a given time and to calculate its primary spacing (i.e., the mean distance between a dendrite tip's center and the centers of its first neighbors). The labels of each dendrite are associated across images so that one dendrite can be followed through the successive images, and its creation, movement, and elimination characterized, as well as the sidebranching development.

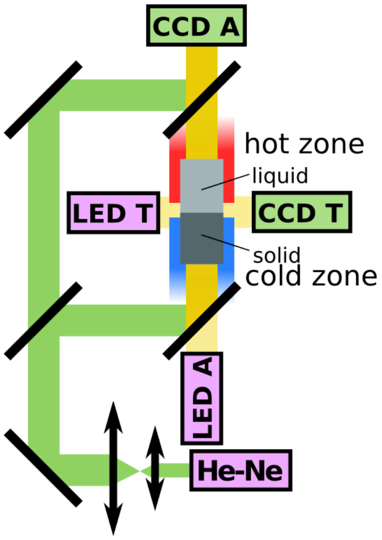

Fig. 1. Experimental setup. A hot and a cold zones (red and blue, respectively) create a thermal gradient in the sample. The light and dark grey rectangles represent the liquid and solid parts of the sample, which is pulled down to induce solidification. Direct optical observation is afforded by the yellow optical paths. Interferometric observation is afforded by the green and dark yellow paths. The labels A and T denote axial and transversal views of the sample, respectively.

3. Image treatment methods for microstructure labelling

When treating axial images, the identification of each dendrite is important, since an error in detection of one dendrite affects the primary spacing measurement of all its neighbors, and erroneous identification of a dendrite in one image can disrupt its cross-image labelling. Each experiment produces several thousand images, each containing hundreds of dendrites, so an automated treatment is necessary.

An extensive search of state of the art did not yield methods to treat real-time bulk transparent alloy images effectively, so we have conceived and developed image binarization methods making extensive use of python programming language libraries [9, 10], first for cellular microstructures [11] and then updated for dendritic patterns, which will be described in this paper.

3.1 Centers identification by threshold masking

This is a simple method interesting for non-concentric features, such as dendrites. One way to detect the centers of the dendrites is to first detect the groove between the dendrites. The raw image is binarized using a threshold value below which we consider the groove. This threshold must be high enough to isolate each dendrite from each other (Fig. 2a). Then a second threshold is applied which takes into account the minimal size that an object must have to be counted as a new center (Fig. 2b).

The combination of both images reliably separates all visible surfaces, even when the interface presents many irregular features: as an example, the superposition of the as-detected centers to the raw image is given in Fig. 2c. The computation is not perfect due to the lack of homogeneity within the image contrast, therefore this method can be coupled, for better results, to the *post* treatment methods (§3.4).

3.2 Centers identification by FFT

The main difficulty encountered in identifying dendrite centers is to distinguish between the main trunk tip and the secondary branches that can exhibit similar brightness. Even after a local equalization rank filter [9] (Fig. 3a), the vast majority of images have features that cannot be binarized by a single threshold value. In order to remove the information on the secondary branches so that the algorithm can focus on the very centers, we apply the Fast Fourier Transform (FFT) on the dispersion image. The dispersion image (Fig. 3b) represents, for each pixel, the standard deviation of the pixel values contained in a patch of a given size and centered on the pixel of interest.

A low-pass filter is then applied to the dispersion image, considering a fixed threshold (in the range of 0 to 1). The goal is to choose a threshold value such that the contour reproduces the canonical shape of the dendrites, which should appear on the FFT (the cross in Fig. 3c). Fig. 3d shows the inverse Fourier Transform of the image with just the low frequencies inside the blue contour of Fig. 3c. Finally, the position of the dendrites can be computed by thresholding this inverse FFT image (Fig. 3e). The value of this threshold is chosen very close to unity to specifically image only tip centers.

The outcome gives satisfying results (Fig. 3f). However, once more, the computation is not perfect due to the lack of homogeneity within the image contrast and this method can be coupled, for better results, to the *post* treatment methods (§3.4).

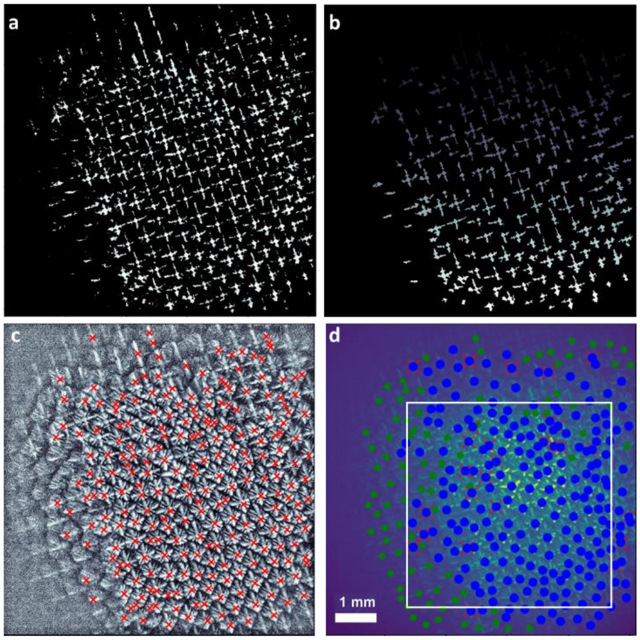

Fig. 2. Intermediary steps produced by the threshold centers identification method: a) Binary image applying a threshold below which we consider the groove); b) Binary image applying a minimal size of these previously isolated dendrites to be counted as a new center; c) centers superimposed to the raw image; d) manual correction that can be made (the green circles represent the centers to add and the red crosses those to delete).

3.3 Characteristic size by FFT

Some images cannot be treated by the previous methods, especially those obtained during the transient step of microstructure formation, because wavelengths and amplitudes are too small for the resolution of our apparatus. Despite this limitation, it is possible to quantify the evolution of the characteristic size of this early interface pattern by analyzing the Fourier spectrograms of the image.

A Fourier transform of a bitmap image in spatial domain maps its characteristics to the frequency domain. Each spatial vector in the Fourier transformed image corresponds to a wave vector of the original image. We make use of the Discrete Fourier Transform (DFT), implemented by the Fast Fourier Transform function in the NumPy library [9] of the Python scripting language.

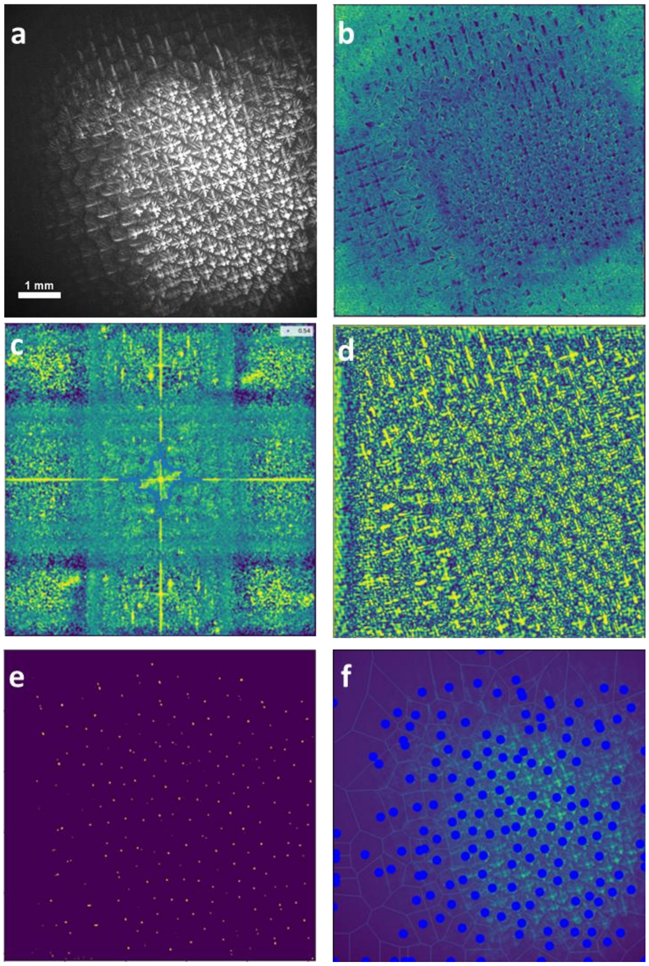

Fig. 3. Intermediary steps produced by the FFT centers identification method: a) Raw image (SCN-0.46wt% camphor, V = 12 µm/s, G = 12 K/cm, after 49 mm of solidification); b) dispersion image; c) FFT on the dispersion image; d) Inverse Fourier Transform of the image with just the low frequencies inside the blue contour of c; e) binary image representing the tip of the dendrites from applying a threshold on d; f) centers and segmentation superimposed to the raw image.

This procedure computes the FFT image of the whole interface, or a squared portion of it, and plots the radially averaged power spectrum (RAPS) and its derivative. The RAPS is the direction-independent mean spectrum, i.e., the average of all possible directional power spectra. It provides a convenient means to view and compare the information contained in 2-D spectra in 1-D. The frequency axis of the main peak is associated with the primary spacing.

To validate this technique, we use an image with an established dendritic pattern to perform a comparison. The squared region of Fig. 2d was considered, and the results are given in Fig. 4. Fig. 4a shows the FFT image of the squared region as well as the corresponding RAPS. The characteristic distance is estimated to be 395 µm. Fig. 4b shows the histogram of the primary spacings in the same region, after center identification by the threshold method. The spacing is estimated to be 409 ± 56 µm. The distributions obtained from the two different methods are in very good agreement (less than 5 % difference), thus validating the use of the FFT method.

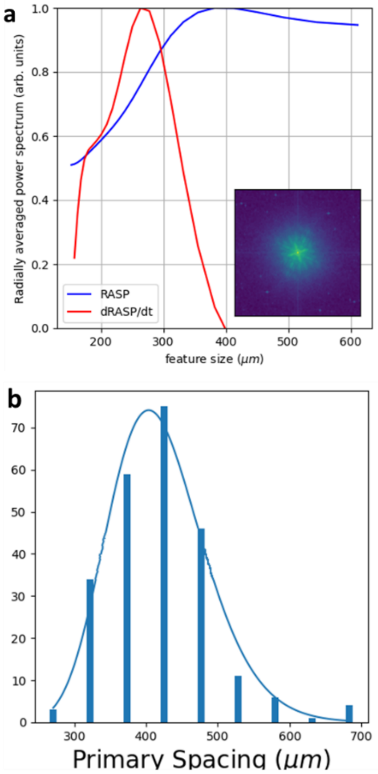

Fig. 4. Characteristic length of the white square zone of Fig. 2d using different techniques. a) Radially averaged power spectrum (RASP) and its derivative. Corresponding FFT image. b) Histogram of the primary spacing after centers detection by thresholding method.

3.4 Post-treatment

The input to the methods described in §3.1 and 3.2 is a greyscale image, and the output is a set of coordinates of the dendrite centers. As previously mentioned, producing an efficient center finder algorithm is difficult. A way to successfully recover the dendrites centers is to first slightly overestimate the center detection and then to remove the redundant centers. A procedure was developed that extracts each individual dendrite's shape over the whole interface, and from all the centers pointing to the same extracted shape, only the one closest to the shape centroid is kept. This time-consuming procedure is combined with the previously defined center identification procedures.

It is also possible to manually interfere in the output containing the centers to delete a center that has been erroneously counted or add a center that was not counted. The corrections are done through the raw image with the centers superimposed. Fig. 2d shows an example where the centers are plotted in blue; the red crosses represent coordinates to delete; the green circles coordinates to add.

The procedure of finding the centers is repeated for each successive image of the interface, to obtain a large set of coordinates in x, y, and t.

Then, a powerful clustering algorithm DBSCAN [10, 12] is used to link the label of each dendrite through time. It will consider all the centers (from all the images) as a 3D scatter plot, and it will try to isolate individual clusters from the rest. The (x(t), y(t)) succession of coordinates of each dendrite is used to calculate its top-view apparent velocity (defined as drift velocity). The clusters computation also helps to correct erroneous identification during the computation of centers. Fig. 5a shows an example where the centers detected by the FFT or thresholding methods (in blue) are compared to the ones resulting from the clusters computation (in red). Using the basic methods, the dendrites surrounded in green had two centers detected, and those surrounded in cyan were not detected. After, the clusters computation, they are correctly considered.

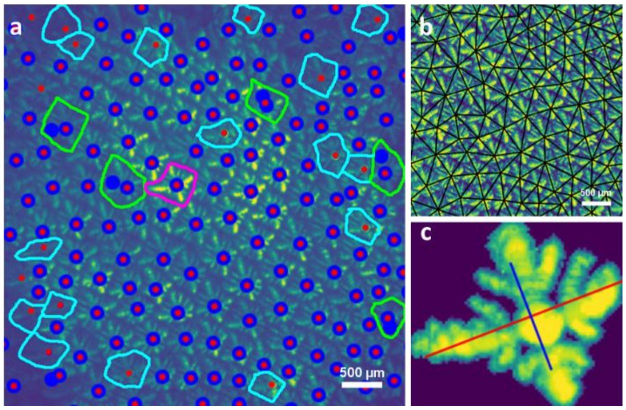

Fig. 5. (a) Comparison between the centers detected by the classical methods (in blue) and the clusters computation (in red) leading to several improvements: the dendrites surrounded in green were overestimated by the classical methods and in cyan not detected. (b) Zoom on the central region with the Voronoi triangulation from the centers of dendrites. (c) Extracted shape of the dendrite surrounded in pink in (a).

After the segmentation and time-labelling of each experiment, the information necessary to extract the physical characteristics with interest and to follow their evolution in time are available. In our case, the methods allow identification of each dendrite center, and a Voronoi tessellation of their centers reliably finds their first neighbors (see example in Fig. 5b). A database of first neighbors, the primary spacing of each dendrite, and the position of each dendrite at all times during the experiment are obtained. The maps of number of neighbors of each dendrite, dendrite position in time, velocity, and primary spacing are then calculated. Furthermore, precise statistics and their evolution on the entire interface or by region can be calculated.

3.4 Local image treatment

Local image treatments are also developed, for example, to analyze an individual dendrite's shape. Fig. 5c shows an example of shape extraction of the dendrite surrounded in pink in Fig. 5a with the corresponding eigenvectors drawn. These eigenvectors enable computation of the orientation of the dendrites. For this particular dendrite, the angle of its principal eigenvector (defined by the red line with respect to the horizontal) is 21°. The shape extraction is performed using a threshold definition.

Another treatment was developed to estimate the frequency of sidebranching emission. For a given dendrite, a sequence of close images is taken. A line of sight is drawn in an angular position delimited by the segments [(x0,y0),(x1,y1)] and [(x0,y0),(x2,y2)] as exemplified in Fig. 6a for a given image. For each line of sight, the peaks and grooves are identified which will define the fringes (black dots in Fig. 6a). From these detections, the "real" fringes are identified by applying the hypothesis: if the line of sight has more than a given percentage of detections within a circle of a given radius, it is considered as "real". In Fig. 6b the detections corresponding to Fig. 6a are represented, but only three of them are "real" fringes. The method output consists of the evolution of the position of the first fringe detected with time and the FFT of this signal reveals the frequency of the appearance of new fringes (in case the phenomenon is periodical). For this particular example, the natural frequency of sidebranching was estimated to be 85 s.

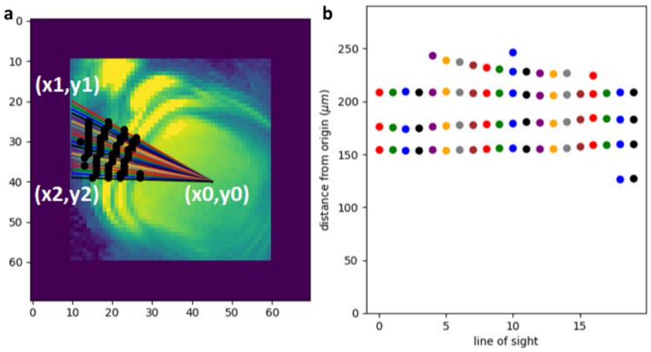

Fig. 6. (a) Extracted dendrite with the different lines of sight and the fringe detection plotted. (b) Representation of the detections for each line of sight as their distance to the center (x0,y0).

4. Results

To illustrate the use of the methods described above, let us analyze an experiment performed onboard ISS at $V = 3$ µm/s and $G = 12$ K/cm. The microstructure formation is quite similar regardless of the type of experiments [13, 14]. After motion is triggered, the morphological instability first initiates along sub-boundaries before developing as a uniform corrugation. The amplitude of all interface modulations increases and grooves start to form, but it is still difficult to identify dendrites. At this stage, the interface dynamics is remarkably fast and the pattern disorder high. There is then a progressive decrease in disorder, and a clear pattern of dendrites eventually emerges (Fig. 7a). The dynamics then slows down and is limited to progressive size adjustments and array ordering. The pattern obtained at the end of solidification is shown in Fig. 7c. The number of nearest neighbors is also determined, which gives information on the quantity of topological defects in the pattern: a perfect hexagonal tiling would correspond to six nearest neighbors for each cell. Fig. 7b and d show the map of nearest neighbors at the beginning and at steady-state: there is a high number of topological defects that are mainly instances of five and seven nearest neighbors. Such penta-hepta defects are commonly observed both experimentally [15, 16] and computationally [17] in disordered hexagonal cellular array patterns formed during directional olidification. More broadly, they are characteristic defects of hexagonal patterns formed in a wide variety of non-equilibrium systems in fluid dynamics, optics, and chemical kinetics [18-20].

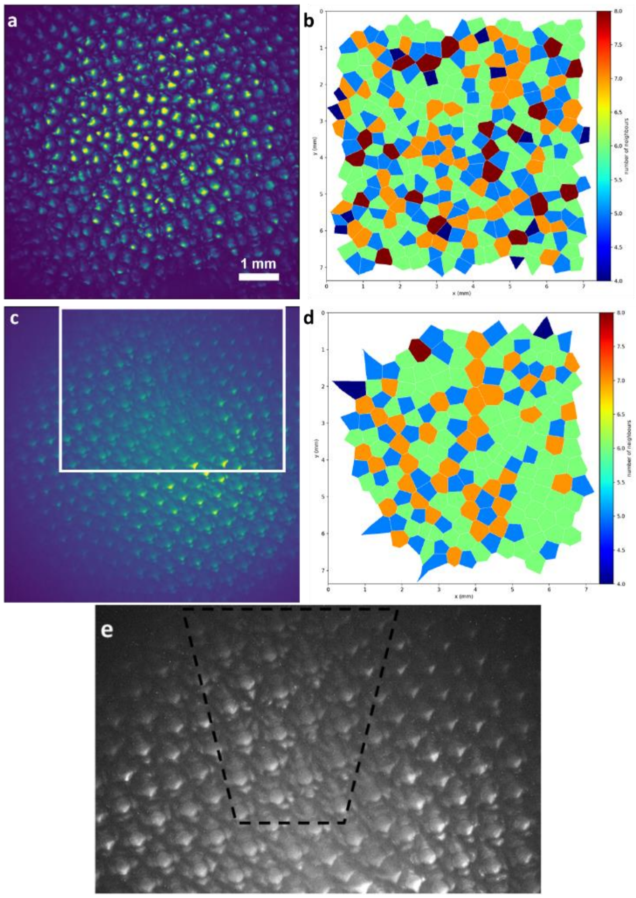

Fig. 7. Top view of the solid-liquid interface and the corresponding maps of nearest neighbors after 6 mm (a and b) and 59 mm (c and d) of solidification. (e) Zoom on the white square of c evidencing the development of secondary branches. (SCN–0.46 wt% camphor, $V = 3$ µm/s, $G = 12$ K/cm).

The possibility of *in situ* visualization of the solidification allows the characterization of the patterns as a function of time. The primary spacing λ, one of the most fundamental characteristics, is for example followed during the whole solidification. We calculate the primary spacing of each dendrite and study the evolution of its average value. Fig. 8 shows the primary spacing (mean and standard deviation) as a function of time. The data points after 24 minutes (L = 4 mm), λ = 384 µm, were obtained applying the procedures of dendrite centers identification presented in §3.1 and 3.2, as the dendritic pattern is sufficiently developed. However, at the early stages of microstructure formation, it is not possible to determine the spacing with center-to-center methods because the grooves between primary dendrites are not deep enough. Therefore, the initial estimation of the average λ is performed using the fast Fourier transform (FFT) analysis (§3.3). The FFT analysis only pertains to the early stage, i.e., at most the first seven data points in Fig. 8 (empty triangles), and is found to provide a good continuity and overlap with the more accurate center to center analysis where both methods are applicable.

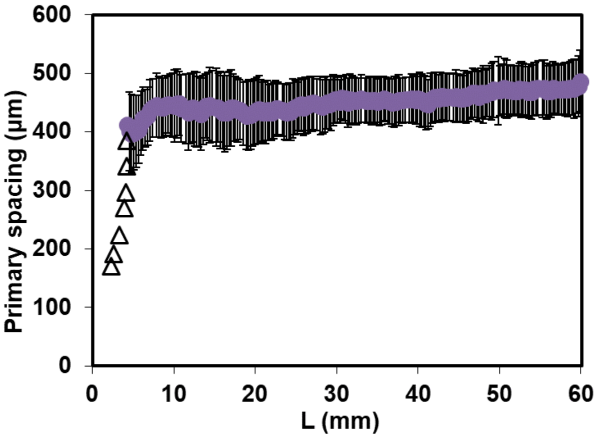

Fig. 8. Primary spacing evolution as a function of the solidified length. (SCN–0.46 wt% camphor, V = 3 µm/s, G = 12 K/cm)

The image sequence reveals dendrites that drift along the interface. In top-view images, the dendrite drift originates in a tilt of the growth direction compared to the pulling direction, meaning that a growth velocity component exists in the plane of the image. It was shown by Deschamps *et al*. [21] that the growth direction lies between two important limits: the direction of the thermal gradient, which is normal to the interface, and a crystallographic preferred growth direction (<100> for our material). As soon as one of these two directions is not perfectly superposed to the pulling axis, as is usually the case, a drift of pattern occurs.

For this experiment, the primary spacing remains stable after the initial transient, and the drift velocity is quite homogeneous along the interface. Trajectories of dendrites are represented for a duration of 4 hours (from 14 to 57 mm of solidification) in Figure 9a. During this time interval, the collective drift caused by the misorientation between the crystal <100> and the pulling axis is evidenced. The average amplitude of drift velocity $\overrightarrow{V_d}$ is used to evaluate the tilt angle θ_g between the growth velocity and the interface velocity, as described in [14]. The amplitude of drift velocity and tilt angle are given for different regions of the interface in the insets of Fig. 9a: they are very close to each other, with a small increase from top to bottom.

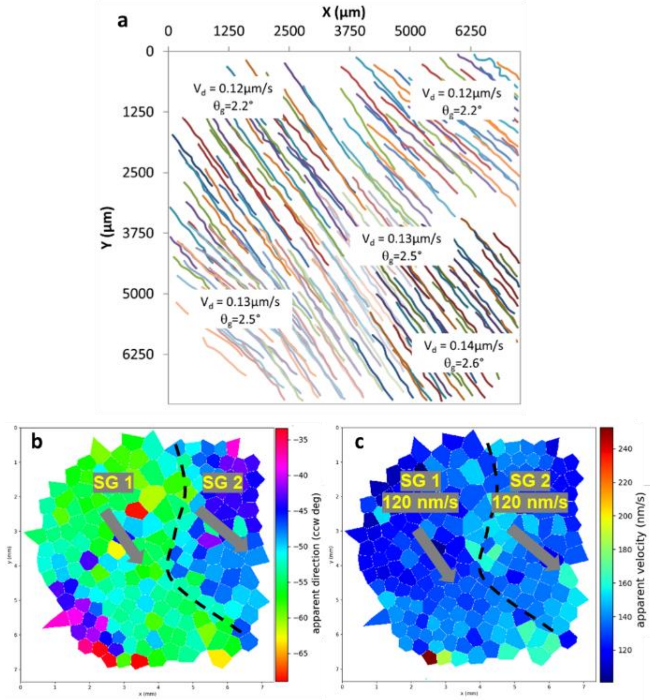

Fig. 9. (a) Trajectories of the dendrites between 1.3 (14) and 5.3 h (57 mm). (b) Drifting direction and (c) velocity amplitude maps at 50 mm. The dashed line corresponds to the sub-boundary (SCN–0.46 wt% camphor, V = 3 µm/s, G = 12 K/cm)

The misorientation of a sub-grain is defined by the angle θ_o between the preferred <100> growth direction and the thermal gradient G. The growth direction, characterized by the tilt angle θ_g, varies relatively to θ_o, and this variation depends on the Péclet number $Pe = \lambda V/D$, where λ is the primary spacing and D is the solute diffusion coefficient in the liquid [21-24]:

$$\frac{\theta_o - \theta_g}{\theta_o} = \frac{1}{1 + f Pe^g} \qquad (1)$$

where f and g constants. 3D phase-field simulations were used to determine the f and g constants associated with alloy composition and experimental parameters by using the method described in [14]. Based on the measured average primary spacing $\overline{\lambda} = 468\,\mu m$ and the average drifting velocity $\overline{V_d} = 0.13\,\mu m/s$ the crystal misorientation θ_o is evaluated to 2.7°.

The time evolution of the primary spacing map extracted from the image sequence is presented in Fig. 10. At the beginning (6 mm), the spacing is highly dispersed all along the interface. As growth progresses, dispersion progressively decreases and there is no clear evidence of ordered variation of spacing, except a line of larger spacings at the top center (clearly distinguished at 59 mm). The origin of this local higher spacing is the existence of a divergent sub-boundary (SB), similar to what was previously found in the cellular regime [14].

The only obvious way to identify sub-grains (SGs), and therefore sub-boundaries (SB), is to analyze the trajectories of dendrites: each SG is characterized by a collective drift of dendrites, of specific direction and amplitude, caused by its particular misalignment to the pulling/thermal axis. The experiment at V = 3 µm/s falls in this category: the microstructure is not strikingly different within the interface, but we notice the presence of areas characterized by different drifting directions, and the different SGs are identified by grouping dendrites with similar drifting directions. Fig. 9b and c show each dendrite velocity magnitude and direction, respectively, after around 50 mm of solidification. Due to small misorientations, both directions and amplitudes are required to discriminate the SGs, and several successive images may be used to validate the location of SBs, which are freehand drawn on Fig. 9b and c. Sub-grains are then named as indicated. The dendrites of SGs 1 and 2 move in slightly different directions: approximately −45° (measured counter-clockwise with right = 0°) for SG2 and -55° for SG1. This motion leads to a local stretching of microstructures, and consequently a line of local higher spacing as evidenced in Fig. 10, and also the development of secondary branches (Fig. 7e).

5. Conclusion

To conclude, these microgravity experiments provided a unique opportunity to observe for the first time the formation and evolution of directionally solidified 2D extended arrays of dendrites in diffusive transport conditions. We have developed a methodology to robustly analyze extremely large datasets obtained from our experiments on board the ISS. These procedures allow us to quantitatively study the complex microstructure dynamics that occur at the solidification interface in a diffusive regime. This is illustrated with an experiment where a dendritic pattern was obtained for a macroscopically flat interface. Understanding the dynamics of pattern formation is a promising challenge, and the microgravity environment allows us to address fundamental phenomena that arise during large-scale bulk solidification, from both numerical and experimental points of view. To this end, the quantitative and powerful methods of data treatment that we have developed are invaluable tools. In addition to providing insight into the dynamics of interface pattern formation, the dendritic microstructural patterns that evolve have direct technological relevance for the solidification and casting industry.

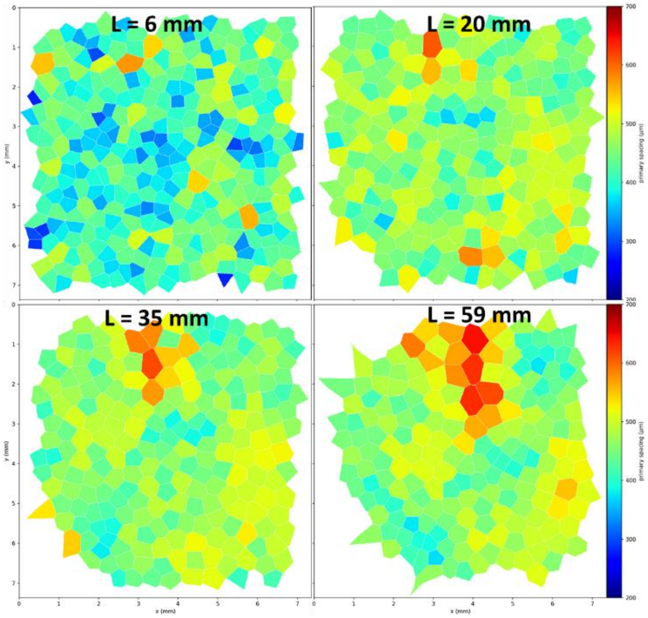

Fig. 10. Primary spacing maps from 6 to 59 mm of solidification (0.5 to 5.4 h). (SCN–0.46 wt% camphor, V = 3 µm/s, G = 12 K/cm).

6. Acknowledgements

This project is supported by the French Space Agency CNES (Microstructures de solidification 3D - MISOL3D – project) and NASA (grants 80NSSC19K0135 and NNX16AL77G - Spatiotemporal Evolution of Three-Dimensional Dendritic Array Structures - SPADES – project).

References

[1] H. Jamgotchian, N. Bergeon, D. Benielli, P. Voge, B. Billia, R. Guerin, Phys. Rev. Lett. 87 (2001) 6105.
[2] T. Schenk, H. Nguyen-Thi, J. Gastaldi, G. Reinhart, V. Cristiglio, N. Mangelinck-Noel, H. Klein, J. Hartwig, B. Grushko, B. Billia, J. Baruchel, J. Cryst. Growth 275 (2005) 201.

[3] F. L. Mota, Y. Song, J. Pereda, B. Billia, D. Tourret, J. M. Debierre, R. Trivedi, A. Karma, N. Bergeon, JOM 69 (2017) 1280.

[4] N. Bergeon, F. L. Mota, J. Pereda, D. Tourret, Y. Song, J. M. Debierre, R. Guerin, A. Karma, R. Trivedi, B. Billia, Int. J. Microgravity Sci. Appl. 33 (2016) 6.

[5] R. Marcout, G. Raymond, B. Martin, G. Cambon, B. Zappoli, F. Duclos, S. Barde, D. Beysens, Y. Garrabos, C. Lecoutre, B. Billia, N. Bergeon, N. Mangelinck, in 57th International Astronautical Congress, Valencia, Spain, 2006.

[6] G. Pont, S. Barde, B. Zappoli, F. Duclos, Y. Garrabos, C. Lecoutre, D. Beysens, B. Billia, N. Bergeon, N. Mangelinck, R. Marcout, D. Blonde, in 60th International Astronautical Congress, Daejeon, Republic of Korea, 2009.

[7] N. Bergeon, C. Weiss, N. Mangelinck-Noel, B. Billia, Trans. Ind. Inst. Met. 62 (2009) 455.

[8] H. Jamgotchian, N. Bergeon, D. Benielli, P. Voge, B. Billia, J. Microsc. 203 (2001) 119.

[9] S. van der Walt, S. C. Colbert, G. Varoquaux, Computing in Science & Engineering 13 (2011) 22.

[10] F. Pedregosa, G. Varoquaux, A. Gramfort, V. Michel, B. Thirion, O. Grisel, M. Blondel, P. Prettenhofer, R. Weiss, V. Dubourg, J. Vanderplas, A. Passos, D. Cournapeau, M. Brucher, M. Perrot, E. Duchesnay, J Mach Learn Res 12 (2011) 2825.

[11] J. Pereda, Y. Song, F. L. Mota, B. Billia, J.-M. Debierre, R. Guerin, A. Karma, R. Trivedi, N. Bergeon, in 67th International Astronautical Congress, Guadalajara, Mexico, 2016.

[12] R. J. G. B. Campello, D. Moulavi, J. Sander, Springer Berlin Heidelberg, Berlin, Heidelberg, 2013, p. 160.

[13] N. Bergeon, F. L. Mota, L. Chen, D. Tourret, J. M. Debierre, R. Guerin, A. Karma, B. Billia, R. Trivedi, IOP Conf. Series: Mat. Sci. Eng. 84 (2015) 012077.

[14] F. L. Mota, J. Pereda, K. Ji, Y. Song, R. Trivedi, A. Karma, N. Bergeon, Acta Mater. 204 (2021) 116500.

[15] B. Billia, H. Jamgotchian, H. N. Thi, Metall. Trans. A 22 (1991) 3041.

[16] J. Pereda, F. L. Mota, L. Chen, B. Billia, D. Tourret, Y. Song, J.-M. Debierre, R. Guerin, A. Karma, R. Trivedi, N. Bergeon, Phys. Rev. E 95 (2017) 012803.

[17] T. Takaki, S. Sakane, M. Ohno, Y. Shibuta, T. Shimokawabe, T. Aoki, Acta Mater. 118 (2016) 230.

[18] E. Bodenschatz, J. R. Debruyn, G. Ahlers, D. S. Cannell, Phys. Rev. Lett. 67 (1991) 3078.

[19] W. J. Firth, P Soc Photo-Opt Ins 2039 (1993) 290.

[20] Q. Ouyang, H. L. Swinney, Nature 352 (1991) 610.

[21] J. Deschamps, M. Georgelin, A. Pocheau, Phys. Rev. E 78 (2008) 1605.

[22] S. Akamatsu, T. Ihle, Phys. Rev. E 56 (1997) 4479.

[23] J. Ghmadh, J.-M. Debierre, J. Deschamps, M. Georgelin, R. Guérin, A. Pocheau, Acta Mater. 74 (2014) 255.

[24] Y. Song, S. Akamatsu, S. Bottin-Rousseau, A. Karma, Phys Rev Mater 2 (2018)